ChemComm

ROYAL SOCIETY OF CHEMISTRY

COMMUNICATION

View Article Online
View Journal | View Issue

Cite this: *Chem. Commun.*, 2025, **61**, 6627

Received 20th February 2025,
Accepted 27th March 2025

DOI: 10.1039/d5cc00888c

rsc.li/chemcomm

A novel cathode Li-supplement additive for high-energy and long-lifespan LIBs†

Chengsifan Lei,[ab] Meng Huang,*[ab] Jinghui Chen,[ab] Feng Tao,[ab] Lei Zhang*[ab] and Qinyou An *[ab]

A novel cathode Li-supplement additive, Li_4SiO_4@rGO, has been developed; it features high capacity (820 mA h g^{-1}), high air stability, and feasible Li-supplement potential (4.3 V). Its integration in NCM622‖graphite improves the energy density by 9% and enhances the capacity retention from 27.5% to 70%. Analogous improvements are also manifested in LFP‖graphite.

Lithium-ion batteries (LIBs) are widely used in electronic devices, energy storage systems, and electric vehicles.[1,2] However, issues such as solid electrolyte interphase (SEI) formation and dead lithium lead to poor coulombic efficiency (CE), low energy density, and capacity fading.[3–6] To achieve high energy density and long cycle life, active lithium supplements are essential. They can be divided into two categories: anode pre-lithiation and cathode supplement additives. Cathode supplement additives offer a simple, cost-effective, and highly compatible solution for lithium supplementation.[7,8] Unlike anode pre-lithiation, which is costly and environmentally unstable, this technology integrates seamlessly into existing production, reducing setup time and operational complexity while using more affordable materials.[9,10] Cathode additives release lithium ions within the cathode material, significantly improving the performance and lifespan of LIBs. Recent advancements in this technology have greatly enhanced LIB performance, making it a promising solution for improving energy density, lifespan, and overall efficiency.[11–13]

Common cathode supplement additives include small-molecule lithium salts, transition metal–lithium salt composites, metal oxide lithium salts, and organic lithium salts.[14] Small molecule lithium salts such as Li_2O,[15] Li_3N,[16] Li_2O_2,[17] and Li_2S[18] offer high irreversible capacity but are highly unstable in air. Gases (*e.g.*, O_2, N_2) or harmful by-products (*e.g.*, H_2S) will be released, ultimately degrading LIB performance. To mitigate oxygen release, these salts are often combined with transition metals, like Fe and LiF,[19] which improve stability but introduce inactive FeF_3, leading to shorter cycle life. Metal oxide lithium salts, Li_5FeO_4[20] and Li_2NiO_2[21] for instance, also suffer from air instability and supplement limited active lithium, restricting their practical use. In recent studies, organic lithium salts like $Li_2C_4O_4$[22] have drawn attention for their air stability, though they suffer from low irreversible capacity. Li_2CO_3, while offering better thermal stability, still faces low capacity and high decomposition voltage, reducing commercial viability.[23] These limitations underscore the need for cathode supplement additives that are compatible with commercial electrodes, offer high capacity, and exhibit superior environmental stability. Herein, we developed a novel cathode Li-supplement additive composed of Li_4SiO_4 (LSO) core particles and a reduced graphene oxide (rGO) coating layer (LSO@rGO), to mitigate the issue of active lithium consumption associated with a SEI.

The obtained LSO, belonging to the monoclinic system, has a unit cell with two SiO_4 tetrahedra connected by Li^+, forming a three-dimensional framework that facilitates Li^+ mobility. However, it exhibits low electronic conductivity, making LSO a poor electronic conductor and a good ionic conductor, but an electrical insulator.[24] To enhance its electronic conductivity, ball milling was employed to reduce the particle size and increase the surface area, followed by spray drying to coat the surface of LSO with rGO, which exhibits excellent electronic conductivity. The process is illustrated in the flowchart shown in Fig. 1a.[25] The scanning electron microscope (SEM) image of the LSO@rGO composite spheres (Fig. 1b) shows a uniform size distribution and better sphericity compared to bulk LSO obtained from solid-phase sintering.

LSO morphology and structure were analyzed using SEM, transmission electron microscopy (TEM), and X-ray diffraction (XRD). TEM-EDS mapping (Fig. 1c and d) shows uniform carbon distribution at the edges of LSO@rGO, confirming

[a] *Sanya Science and Education Innovation Park of Wuhan University of Technology, Sanya, 572000, P. R. China. E-mail: anqinyou86@whut.edu.cn*
[b] *State Key Laboratory of Advanced Technology for Materials Synthesis and Processing, Wuhan University of Technology, Wuhan, 430070, P. R. China*

† Electronic supplementary information (ESI) available. See DOI: https://doi.org/10.1039/d5cc00888c

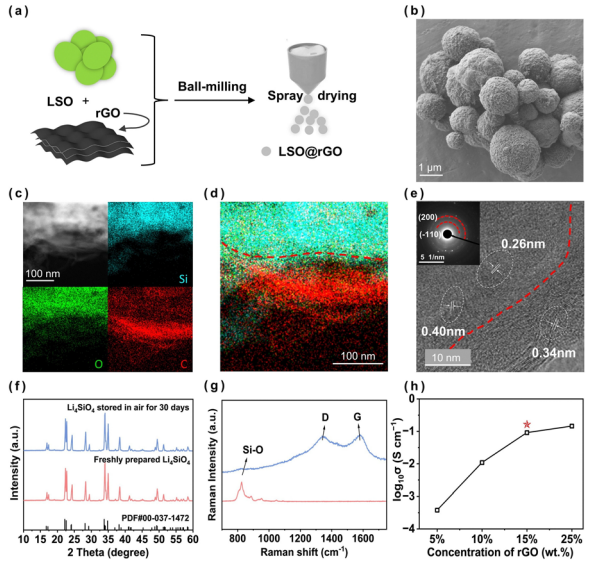

Fig. 1 (a) Fabrication of LSO@rGO spheres. (b) SEM images. (c, d) HR-TEM, mapping, and elemental overlay (Si, C, O). (e) Lattice fringes. (f) XRD of fresh and air-stored LSO. (g) Raman spectra. (h) Conductivity of LSO@rGO *vs.* rGO concentration.

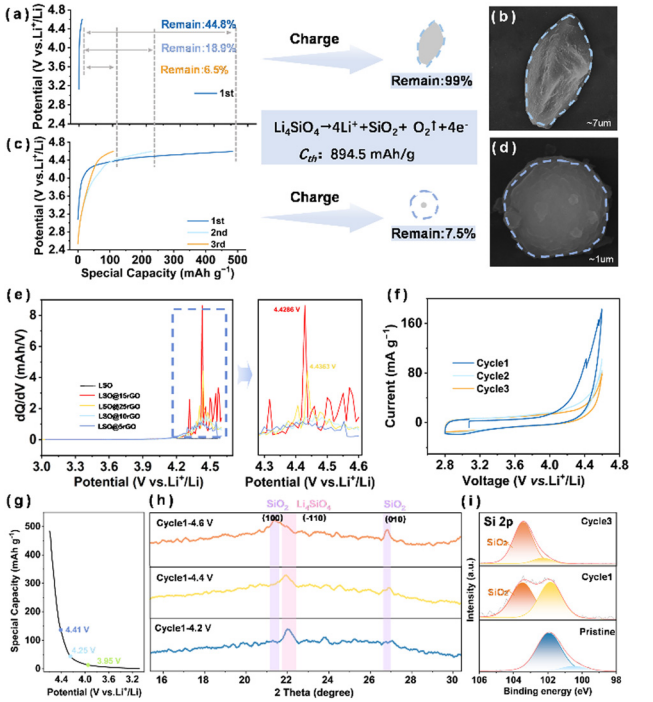

Fig. 2 (a, c) Charge–discharge curves and schematics of LSO and LSO@rGO (0.05C). (b, d) SEM images of LSO and LSO@rGO. (e) d*Q*/d*V* curves of LSO@rGO. (f) CV curves of LSO@rGO. (g) Charge–discharge profiles of LSO@rGO. (h, i) *Ex situ* XRD and XPS (Si 2p) spectra of LSO@rGO.

successful rGO coating. Fourier analysis reveals lattice spacings of 0.26 nm and 0.40 nm, corresponding to LSO's (200) and (−110) planes, and 0.34 nm at the edges, matching with the (002) plane of rGO (Fig. 1e). XRD confirms LSO's monoclinic structure with peaks at 11.1°, 11.3°, and 16.7°, and minimal changes after 30 days in humid air, indicating excellent stability (Fig. 1f). To investigate the chemical stability of LSO@rGO, we soaked the material in NMP for 24 hours. After drying, XRD analysis (Fig. S1, ESI†) showed no impurities. Thermogravimetric analysis (Fig. S2, ESI†) shows negligible mass loss for LSO from 30 to 800 °C, indicating superior thermal stability. LSO@rGO exhibits slight weight loss below 400 °C due to oxygen group decomposition, with rGO oxidation above 433 °C.[26]

Raman spectra (Fig. 1g) confirm the presence of rGO through D and G peaks, and an additional Si–O peak at 825 cm^{-1}. FTIR (Fig. S3, ESI†) shows C=C and Si–Si vibrations at 1400–1500 cm^{-1} and 1000–1100 cm^{-1}, respectively. Conductivity tests show that increasing rGO from 5 wt% to 25 wt% raises the conductivity from 3.78×10^{-4} S cm^{-1} to 0.14 S cm^{-1}, with the most significant improvement at 15 wt%. Pure LSO has a much lower conductivity of 4.60×10^{-6} S cm^{-1} (Fig. 1h). We also conducted ionic conductivity tests (Fig. S4, ESI†) and compiled the results in Table S1 (ESI†), showing that 15 wt% rGO maintains a balance between electron transport and lithium-ion migration. The specific surface area of LSO@rGO (13.8 m^2 g^{-1}) is significantly larger than that of LSO (1.8 m^2 g^{-1}), enhancing integration and conductive network formation (Fig. S5, ESI†). This highlights rGO's dual role in improving conductivity and surface area.

Fig. 2(a) shows the galvanostatic charge–discharge curves of LSO at 0.05C (1C = 894.5 mA h g^{-1}) with a 4.6 V cut-off, and capacity release only happens in the first cycle. Only 9.71 mA h g^{-1} is obtained, indicating that only 1% of Li^+ is extracted due to large particle size (~7 μm, Fig. 2(b)) and poor electrical conductivity. In contrast, LSO@rGO, with smaller particles (~1 μm, Fig. 2(d)), exhibits significantly improved performance. Under the same conditions (Fig. 2(c)), LSO@rGO delivers capacities of 485 mA h g^{-1}, 232 mA h g^{-1}, and 111 mA h g^{-1} in the first three cycles, and only 7.5% of the capacity remains unreleased. Therefore, ~92.5% of LSO@rGO's Li-supplement capacity is efficiently utilized, highlighting its excellent performance as a lithium supplement additive. The d*Q*/d*V* curve in Fig. 2(e) shows that Li supplement potential (average delithiation potential) of LSO@rGO remains stable at ~4.43 V as the rGO content increases from 5 wt% to 25 wt%, and the sharpest oxidation peak is observed when rGO is at 15 wt%. Pristine LSO, without rGO coating, shows no discernible decomposition peak, suggesting that rGO improves conductivity and facilitates delithiation. The CV profile in Fig. 2(f) reveals a prominent oxidation peak at 4.42 V, indicating progressive Li^+ extraction from LSO@rGO, and a minimal reduction peak, which diminishes with cycling. These results reveal that rGO contributes negligible capacity (less than 0.37% of the total capacity) (~820 mA h g^{-1}) (Fig. S6, ESI†), and primarily enhances electronic conductivity.

To investigate the electrochemical properties of the LSO@rGO electrodes, half-cells were tested with *ex situ* XRD and XPS. XRD shows a decrease in the LSO (−110) peak at 11.1° upon charging from 4.2 to 4.6 V (Fig. 2(g) and (h)), while SiO_2 peaks at 10.4° (100) and 13.3° (011) increase. The Si 2p spectrum

(Fig. 2(i)) shows a reduction in the 101.9 eV peak (LSO) and a new peak at 103.5 eV (SiO_2) is generated during charging. After three cycles, the 101.9 eV peak disappears, confirming irreversible Li-extraction from LSO@rGO.

To assess LSO@rGO as a cathode additive, it was incorporated into NCM622 and LFP cathodes. Electrochemical performance was tested within a 2.8–4.6 V range at 0.2C (1C = 174.5 mA h g^{-1}). The first three charge capacities for NCM622/LSO@rGO‖Li are 240.2, 213.5, and 204.5 mA h g^{-1}, while those for NCM622‖Li are 231.7, 203.8, and 198.7 mA h g^{-1}, respectively. The corresponding capacity enhancements are 8.5, 9.7, and 5.8 mA h g^{-1} (Fig. 3a), resulting in a 3% improvement in specific discharge capacity by the fourth cycle. CV measurements (Fig. 3(b and c)) show a distinct shift in the oxidation peak of NCM622/LSO@rGO during the first cycle, indicating slower Li^+ migration and increased polarization. In subsequent cycles, NCM622/LSO@rGO outperforms NCM622/LSO in oxidation–reduction peaks. Electrochemical impedance spectroscopy (Fig. S7, ESI†) shows lower charge transfer impedance for NCM622/LSO@rGO‖Li, suggesting better electronic conductivity.

Rate and cycling performance are shown in Fig. 3(d and e). The NCM622/LSO@rGO‖Li half-cell delivers 160.8 mA h g^{-1} at 1C, maintaining 101.2 mA h g^{-1} at 15C, whereas the NCM622‖Li half-cell delivers 142.3 mA h g^{-1} at 1C and 76.3 mA h g^{-1} at 15C. This demonstrates that LSO@rGO increases both overall capacity and high-rate performance. Cycling performance in Fig. 3(e) shows that NCM622/LSO@rGO‖Li retains 84% of its initial capacity (223.9 mA h g^{-1}) after 100 cycles at 1C, while NCM622‖Li drops from 193.3 mA h g^{-1} to 153.7 mA h g^{-1} (80% retention). The improved retention is attributed to the Li^+ supplement from LSO and enhanced ionic and electronic conductivity from rGO.

Furthermore, the performance of LSO@rGO in lithium iron phosphate (LFP) electrodes was examined. In the 2.5–4.6 V range at 0.2C (1C = 170 mA h g^{-1}), the LFP/LSO@rGO‖Li half-cell shows an initial charge capacity of 197.0 mA h g^{-1}, outperforming LFP‖Li (169.6 mA h g^{-1})—an increase by 16% (Fig. 3f). CV curves (Fig. 3(g and h)) reveal a distinct oxidation peak at 4.0 V, with the intensity increasing in subsequent cycles. EIS data (Fig. S8, ESI†) confirms lower charge transfer impedance for LFP/LSO@rGO‖Li, indicating improved conductivity. Rate and cycling performance are shown in Fig. 3(i and j). As the rate increases from 0.3C to 20C (Fig. 3(i)), LFP/LSO@rGO‖Li maintains 159.0 mA h g^{-1} at 0.3C but drops to 94.0 mA h g^{-1} at 20C, while LFP‖Li decreases from 155.5 mA h g^{-1} to 87.0 mA h g^{-1}. This highlights the improved high-rate performance of LFP/LSO@rGO. Over 100 cycles (Fig. 3(j)), after one cycle of pre-cycling at 0.2C, the specific capacity of LFP/LSO@rGO‖Li at 0.5C is 152.5 mA h g^{-1}, which remains at 149.9 mA h g^{-1} after 100 cycles, resulting in a capacity retention of 98.3%. In contrast, LFP‖Li decreases from 149.7 mA h g^{-1} to 146.1 mA h g^{-1}, corresponding to a low capacity retention of 97.5%. Additionally, LFP/LSO@rGO‖Li maintains a higher CE above 99.4%, while LFP‖Li ranges between 97% and 98%. These improvements are attributed to the Li^+ supplement from LSO and enhanced ion transport and electronic conductivity from rGO, which probably offsets the adverse effects of the insulator SiO_2 (Fig. S9, ESI†).[27]

To further assess the applicability of LSO@rGO as a cathode supplement additive, the electrochemical performance of full cells with graphite (Gr) anodes and NCM622/LSO@rGO or LFP/LSO@rGO cathodes was investigated. Fig. S10 (ESI†) shows the charge–discharge curves of the Gr anodes, and the initial discharge capacity is 397.0 mA h g^{-1} (0.2C, 1C = 340 mA h g^{-1}), with a reversible capacity of 383.7 mA h g^{-1}. As shown in Fig. 4a, the cells were cycled at 0.2C (1C = 174.5 mA h g^{-1}) within a voltage range of 2.3 to 4.4 V. The initial discharge capacity of NCM622‖Gr is 166.0 mA h g^{-1} with a CE of 79.8%, while NCM622/LSO@rGO‖Gr has a discharge capacity of 180.0 mA h g^{-1} and a higher CE of 82.1%. The third-cycle discharge capacity of the NCM622‖Gr cell is 155.0 mA h g^{-1} (CE = 96.4%), while the NCM622/LSO@rGO‖Gr cell shows a discharge capacity of 174.6 mA h g^{-1} (CE = 96.8%), corresponding to a 9% improvement in energy density (from 444 to 484 W h kg^{-1}). The cycling performance of the NCM622/LSO@rGO‖Gr and NCM622‖Gr cells is shown in Fig. 4b. After 300 cycles at 2C, the capacity of NCM622‖Gr decreases from 156.7 mA h g^{-1} to 43.1 mA h g^{-1}, corresponding to a low capacity retention of 27.5%. In contrast, NCM622/LSO@rGO‖Gr exhibits a more favourable performance, with a decrease from 158.6 mA h g^{-1} to 110.4 mA h g^{-1}, corresponding to a much higher capacity retention of 70%. The significantly improved cyclability of NCM622/LSO@rGO‖Gr emphasizes the beneficial effects of LSO@rGO in enhancing Li supplements. Fig. 4c presents the charge–discharge curves of NCM622/LSO@rGO‖Gr at various rates.

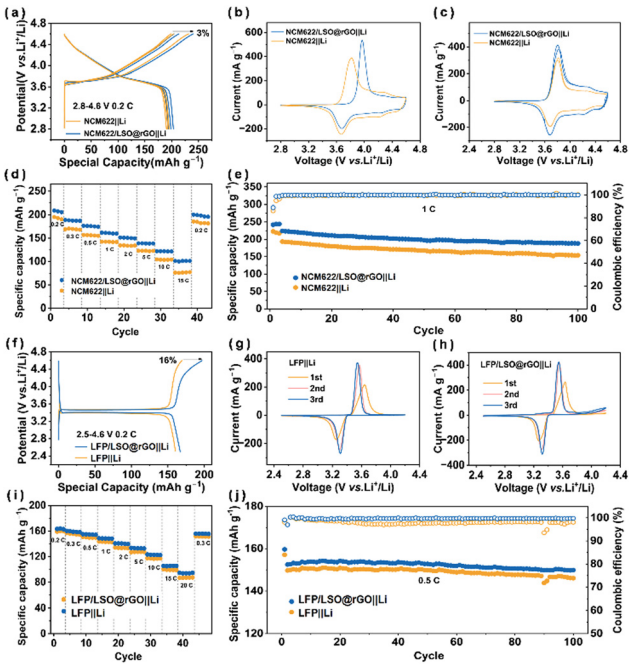

Fig. 3 (a, f) Initial charge–discharge curves of NCM622, NCM622/LSO@rGO, LFP, and LFP/LSO@rGO half-cells. (b, c, g, h) CV curves of NCM622‖Li, NCM622/LSO@rGO‖Li, LFP‖Li, and LFP/LSO@rGO‖Li (first three cycles). (d, i) Rate performance. (e, j) Cycling performance after 0.1C activation, followed by 1C (NCM622) or 0.5C (LFP) cycling.

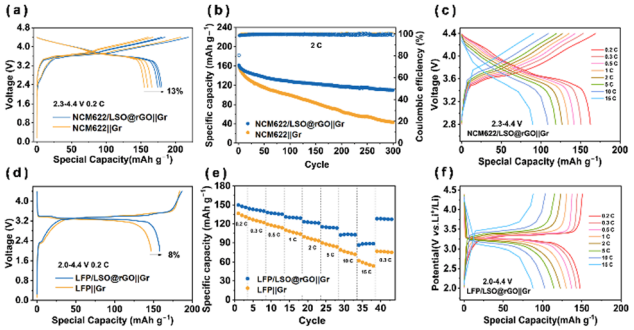

Fig. 4 (a, d) Initial charge–discharge curves of NCM622, NCM622/LSO@rGO, LFP, and LFP/LSO@rGO full cells. (b) Cycling performance at 2C. (c, f) Charge–discharge curves of NCM622/LSO@rGO||Gr and LFP/LSO@rGO at different rates. (e) Rate performance.

Notably, as the rate increases, the voltage polarization rises slowly. Even at a high rate of 10C, a discharge capacity of 108.8 mA h g^{-1} is maintained.

Fig. 4d shows the initial charge–discharge curves of LFP and LFP/LSO@rGO full cells. In the 2.0–4.4 V range, the initial discharge capacity of LFP/LSO@rGO||Gr is 8% higher than that of LFP||Gr, with the CE improved from 80.0% to 84.7%. As depicted in Fig. 4e, the specific capacities of LFP/LSO@rGO||Gr at different C-rates (0.2, 0.3, 0.5, 1, 2, 5, 10, and 15C) range from 147.8 mA h g^{-1} to 88.3 mA h g^{-1}, with a recovery capacity of 127.8 mA h g^{-1} when the rate returns to 0.3C. By contrast, the capacities range from 133.5 to 57.3 mA h g^{-1} for LFP/LSO||Gr with a recovery capacity of 76.4 mA h g^{-1}, and a corresponding rate recovery of only 61.0%. Fig. 4f demonstrates that LFP/LSO@rGO||Gr maintains a stable discharge plateau at 3.24 V at 0.2C, exhibiting a low voltage polarization of 0.100 V. As the charge–discharge rate increases, the polarization increases to 0.35 V at 10C, while the capacity remains at 103.0 mA h g^{-1}. Although LFP||Gr (Fig. S11, ESI†) shows a discharge plateau at 3.28 V at 0.2C, with a polarization of 0.095 V, at 10C, polarization sharply increases to 0.72 V, and the capacity decreases to 77.0 mA h g^{-1}. This reduction in polarization and increase in rate capability for LFP/LSO@rGO||Gr is attributed to the enhanced conductivity of the rGO network, which facilitates more efficient electron transport. Furthermore, compared to LFP||Gr, the LFP/LSO@rGO||Gr cell demonstrates a 7.5% increase in capacity after the first cycle at 0.2C and an 18.5% improvement after 100 cycles (Fig. S12, ESI†). The enhanced capacity, superior cycling stability, and improved rate performance of both NCM622/LSO@rGO||Gr and LFP/LSO@rGO||Gr cells further confirm the effectiveness of LSO@rGO as a Li-supplementing additive.

In summary, a novel cathode Li-supplement additive, LSO@rGO composite, is proposed for improving the electrochemical performance of LIBs. The reduction in the size of Li_4SiO_4, combined with the rGO coating, successfully lowers its Li-supplement potential to approximately 4.3 V. When the LSO@rGO composite is incorporated as a Li-supplement additive, the initial CE of the NCM622/LSO@rGO||Gr full cell increases from 79.8% to 82.1%, the capacity retention after 300 cycles at 2C improves from 27.5% to 70.0%, and the energy density increases from 444 to 484 W h kg^{-1}. Similarly, for the LFP/LSO@rGO||Gr full cell, the initial CE is increased from 80.0% to 84.7%, the improvement in capacity retention is 18.5% after 100 cycles at 0.2C, and the energy density gains a 19% improvement. The significant attributes of LSO@rGO, including low cost, high Li-supplement capacity, compatibility with various cathodes, and excellent chemical stability, make it a promising candidate for advancing the energy density and lifespan of commercial LIBs.

This research was supported by the Project of Sanya Yazhou Bay Science and Technology City (Grant No: SKJC-JYRC-2024-64, SCKJ-JYRC-2023-55), the Science and Technology special fund of Hainan Province (ZDYF2025GXJS008), the National Natural Science Foundation of China (52172231, 52474333, 22409154, 52472246, and 22109123), the Natural Science Foundation of Hubei Province (2022CFA087), and the National Key Research and Development Program of China (2023YFB3809501, 2024YFB3814200).

Data availability

The data supporting this article have been included as part of the ESI.†

Conflicts of interest

There are no conflicts to declare.

Notes and references

1 L. Liang, *et al.*, *Sci. Adv.*, 2024, **10**, eado4472.
2 M. Armand, *et al.*, *Nature*, 2008, **451**, 652–657.
3 C. P. Grey, *et al.*, *Nat. Commun.*, 2020, **11**, 6279.
4 Z. Sun, *et al.*, *Adv. Energy Mater.*, 2024, **14**, 2470009.
5 J. Pu, *et al.*, *Energy Environ. Sci.*, 2021, **14**, 3872–3911.
6 X. Han, *et al.*, *Energy Environ. Sci.*, 2023, **16**, 5395–5408.
7 X. Min, *et al.*, *Energy Storage Mater.*, 2022, **47**, 297–318.
8 R. Zhan, *et al.*, *Adv. Energy Mater.*, 2021, **11**, 2101565.
9 Y. Sun, *et al.*, *Nat. Energy*, 2016, **1**, 15008.
10 M. Cao, *et al.*, *Adv. Funct. Mater.*, 2022, **33**, 2210032.
11 W. Wu, *et al.*, *Small*, 2023, **19**, 2301737.
12 J. Du, *et al.*, *Nano Lett.*, 2020, **20**, 546–552.
13 K. Jun, *et al.*, *Adv. Energy Mater.*, 2023, **13**, 2301132.
14 Z. Huang, *et al.*, *Carbon Energy*, 2022, **4**, 1107–1132.
15 Y. Qiao, *et al.*, *Nat. Energy*, 2021, **6**, 653–662.
16 Y. Sun, *et al.*, *Energy Storage Mater.*, 2017, **6**, 119–124.
17 C. Li, *et al.*, *ACS Appl. Mater. Interfaces*, 2023, **15**, 44921–44931.
18 Y. Zhan, *et al.*, *Electrochim. Acta*, 2017, **255**, 212–219.
19 G. Luo, *et al.*, *Energies*, 2023, **16**, 4232.
20 B. Zhu, *et al.*, *Chem. Sci.*, 2024, **15**, 12879–12888.
21 S. Ding, *et al.*, *Energy Storage Mater.*, 2024, **75**, 103998.
22 G. Liu, *et al.*, *Energy Environ. Sci.*, 2024, **17**, 1163–1174.
23 Y. Zhu, *et al.*, *Adv. Mater.*, 2024, **36**, 2312159.
24 M. Aslam, *et al.*, *Solid State Ionics*, 2016, **293**, 72–76.
25 X. Zhang, *et al.*, *Materials*, 2022, **15**, 4264.
26 G. Wang, *et al.*, *Nano-Micro Lett.*, 2022, **14**, 65.
27 Z. Sun, *et al.*, *Adv. Energy Mater.*, 2025, 2500189.

